Luo *et al. Microstructures* 2023;3:2023011
DOI: 10.20517/microstructures.2022.41

Microstructures

Research Article

Open Access

Check for updates

Triethanolamine assisted synthesis of bimetallic nickel cobalt nitride/nitrogen-doped carbon hollow nanoflowers for supercapacitor

Qiao Luo, Congcong Lu, Lingran Liu, Maiyong Zhu

Research School of Polymeric Materials, School of Materials Science & Engineering, Jiangsu University, Zhenjiang 212013, Jiangsu, China.

Correspondence to: Dr. Maiyong Zhu, Research School of Polymeric Materials, School of Materials Science & Engineering, Jiangsu University, Zhenjiang 212013, Jiangsu, China. E-mail: maiyongzhu@ujs.edu.cn

How to cite this article: Luo Q, Lu C, Liu L, Zhu M. Triethanolamine assisted synthesis of bimetallic nickel cobalt nitride/nitrogen-doped carbon hollow nanoflowers for supercapacitor. *Microstructures* 2023;3:2023011. https://dx.doi.org/10.20517/microstructures.2022.41

Received: 12 Nov 2022 **First Decision:** 8 Dec 2022 **Revised:** 22 Dec 2022 **Accepted:** 13 Jan 2023 **Published:** 30 Jan 2023

Academic Editor: Lianzhou Wang **Copy Editor:** Fangling Lan **Production Editor:** Fangling Lan

Abstract

Supercapacitors (SCs) have drawn growing attention due to their advantages in fast charge/discharge over batteries. Benefiting from their prominent electrical conductivity and metal-like characteristics, transition metal nitrides have emerged as promising electrode materials for SCs. Traditional ways to prepare metal nitrides through ammonolysis are inconvenient and induce severe environmental pollution. Herein, we report a facile synthetic method toward heterogenous Ni_3N-$Co_2N_{0.67}$/nitrogen-doped carbon (Ni_3N-$Co_2N_{0.67}$/NC) hollow nanoflower via pyrolyzing NiCo-TEOA (triethanolamine) complex precursor applying urea as nitrogen source. Electrochemical tests demonstrate that the Ni_3N-$Co_2N_{0.67}$/NC nanoflower delivers good specific capacitance (1582 F g^{-1} at 1 A g^{-1}) and steady cycle performance (83.79% after 5000 cycles). Moreover, the as-assembled Ni_3N-$Co_2N_{0.67}$/NC//AC cell can reach a peak energy density of 32.4 W h kg^{-1} at a power density of 851.3 W kg^{-1}. The excellent electrochemical performance confirms extensive application prospects of the Ni_3N-$Co_2N_{0.67}$/NC nanoflower.

Keywords: Nanoflower, hollow structure, transition metal nitride, nitrogen-doped carbon, supercapacitor

INTRODUCTION

The rapid development of clean and renewable energy in various fields including electric vehicles and

portable electronic devices desires high-efficiency and high-capacity energy storage devices[1,2]. Supercapacitors (SCs) have attracted much interest due to their enhanced power density and long service life[3]. Standing in the intermediate zone of batteries and traditional capacitors, SCs could be generally divided into two types. Electric double-layer capacitors (EDLCs) rely on the electrostatic attraction of ions at the interfaces between electrode and electrolyte to complete charge storage, whereas pseudocapacitors (PCs) take advantage of redox reactions during faradaic redox processes to store electric energies[4,5]. Importantly, developing SCs with stronger energy storage capacity inevitably demands the utilization of better electrode materials[6].

Numerous transition metal nitrides (TMNs) such as Ni_3N[7], Co_2N[8], Fe_2N[9], VN[10] and MoN[11] have emerged as potential electrode materials for SCs by virtue of their distinctive electronic structure, stable chemical resistance, remarkable electric conductivity, and flexible mechanical deformability[12]. However, most of the TMNs are synthesized by pyrolyzing the precursor under NH_3 atmosphere, which leads to massive waste of NH_3 and causes immeasurable environmental pollution. Consequently, there is a desperate need to develop a more convenient and green approach to prepare TMNs. Importantly, applying nontoxic and environmentally friendly nitrogen sources is a priority. Nitrogenous organic small molecules, which are easy to store and can produce NH_3 under high temperatures, might serve as ideal substitutes for NH_3. For example, Yang *et al.* converted vanadium-organic compounds (VAORCS) into vanadium nitride quantum dots/nitrogen-doped hierarchical carbon nanocomposites (VNQD/NDHCs) by annealing the mixture of VAORCS powder and melamine[13]. Jin *et al.* mixed chloride salts of five different metals with urea by ball-milling to form a metal-urea gel and obtained high-entropy metal nitride via calcining the gel[14]. Inspired by these previous reports, we chose urea as the nontoxic and cheap nitrogen source to prepare metal nitrides. In addition, different from individual ones, bimetallic nanoparticles often exhibit higher catalytic activities, richer redox sites, and better chemical stabilities[15-17]. Meanwhile, nickel and cobalt are chosen because they have comparable atomic size and chemical valence state[18].

On the other hand, it is known to all that the most important factor affecting the performance of materials is their morphology and structure. Compared to solid structures, hollow ones possess large inner voids, reactive inner surfaces and indestructible structures[19]. Hence, constructing hollow structures with low mass transport resistance, rapid ion diffusion channels and high-volume electrical capacity stands out as an efficient strategy to enhance SCs performance[20]. Metal-small organic molecule complexes are ideal precursors for hollow structures. Liu *et al.* coordinated Ni^{2+} and Co^{2+} with glycerol and then transformed the solid complex into a yolk-shell structure via the hydrothermal method[21]. Dong *et al.* synthesized hollow carbon spheres by etching SiO_2 template with HF[22]. To avoid the use of a template and multifarious synthesis steps, we designed a one-step strategy toward hollow structure by coordinating Ni^{2+} and Co^{2+} with triethanolamine (TEOA) accompanied by the hydrolysis of metal alkoxide. Meanwhile, the nitrogenous organic network could be pyrolyzed into N-doped carbon via calcine, which further enhances the electrical conductivity and serves as strong support during long-term cycling[23].

Herein, we reported a hierarchical Ni_3N-$Co_2N_{0.67}$/nitrogen-doped carbon (NC) hollow nanoflower, which is derived from annealing nickel/cobalt-TEOA complex (N_1C_2-TEOA) precursor with urea as nitrogen source. The as-prepared Ni_3N-$Co_2N_{0.67}$/NC delivers larger specific surface area, superior energy storage capacity and longer cycle lifespan. The Ni_3N-$Co_2N_{0.67}$/NC transformed from N_1C_2-TEOA sample shows an excellent specific capacitance of 1582 F g^{-1} at 1 A g^{-1} and 83.79% capacitance retention after 5000 cycles. Furthermore, the assembled Ni_3N-$Co_2N_{0.67}$/NC//AC asymmetric device demonstrates a maximum energy density of 32.4 Wh kg^{-1} and steady cycle performance of 95.8% after 5000 cycles.

MATERIALS AND METHODS

Materials

Nickel chloride hexahydrate ($NiCl_2·6H_2O$), Cobalt chloride hexahydrate ($CoCl_2·6H_2O$), triethanolamine (TEOA) and urea were all purchased from Shanghai Aladdin Biochemical Technology Co., Ltd and used without further purification. The deionized water (DI water) involved in the experiment with an electrical resistivity of 18.2 MΩ cm^{-1} was prepared by ultrapure water polishing system.

Sample preparation and characterization

Synthesis of heterogenous Ni3N-Co2N0.67/NC hollow nanoflowers

Firstly, 2 g TEOA was dissolved in 18 mL DI water under vigorous stirring. Subsequently, x mmol $NiCl_2·6H_2O$ and y mmol $CoCl_2·6H_2O$ (x + y = 3, x:y = 0:3, 1:2, 1:1, 2:1, 3:0) were added into the above mixture to form a homogenous solution. The solution was then transferred to a 50 mL Teflon-lined stainless-steel autoclave, which was heated at 160 °C and kept for 12 h. The obtained product was washed with DI water and ethanol three times, respectively. Finally, the product was collected by centrifugation and vacuum dried in an oven for 12 h at 60 °C to obtain N_xC_y-TEOA hollow nanoflowers. The samples are labeled as N_0C_3-TEOA, N_1C_2-TEOA, N_1C_1-TEOA, N_2C_1-TEOA and N_3C_0-TEOA.

The heterogenous Ni_3N-$Co_2N_{0.67}$/NC was synthesized by the following process. Initially, 50 mg N_1C_2-TEOA and 500 mg urea (mass ratio: 1:10) were uniformly dispersed in the porcelain boats. Then the boat with urea and N_1C_2-TEOA was placed upstream and downstream of the tube furnace, respectively. The furnace was heated to 400 °C at a heating rate of 2 °C min^{-1} under N_2 atmosphere and kept for 2 h. After natural cooling down to room temperature, heterogenous Ni_3N-$Co_2N_{0.67}$/NC hollow nanoflowers were obtained.

Structure and morphological characterization

X-ray diffraction (XRD) was tested using Rigaku Ultimate IV powder X-ray diffractometer with Cu Kα radiation (λ = 1.5418 Å) at a scanning speed of 5°/min. Scanning electron microscopy (SEM) was performed on Zeiss sigma 300 scanning electron microscope. Transmission electron microscopy (TEM), high-resolution transmission electron microscopy (HRTEM) and selected area electron diffraction (SAED) were carried out on FEI Talos F200x transmission electron microscope. Brunauer-Emmett-Teller (BET) specific surface areas and pore volumes were measured on ASAP 2460. X-ray photoelectron spectroscopy (XPS) data was collected on Thermo Scientific K-Alpha using Al Ka X-ray as the excitation source (hv = 1486.6 eV). Fourier transform infra-red (FTIR) tests were performed on a FTIR apparatus (Nicolet MX-1E, USA).

Electrochemical characterization

The electrochemical measurements were tested by a three-electrode configuration in 1 M KOH electrolyte. Platinum electrode and saturated calomel electrode were used as the counter electrode and reference electrode, respectively. All the electrochemical performance was studied on a CHI760E electrochemical workstation. The working electrode was fabricated by the following procedures. Active material (Ni_3N-$Co_2N_{0.67}$/NC), polyvinylidene fluoride (PVDF), and acetylene black (mass ratio: 7.5:1:1.5) were homogenously mixed and ground using 1-methyl-2-pyrrolidinone as solvent to form a slurry. The slurry was then uniformly coated on 1 × 1 cm^2 square area of a 1 × 5 cm^2 nickel foam (NF). After vacuum drying in an oven at 60 °C for 12 h, the slurry-coated NF area was pressed under 10 Mpa for 2 min. Finally, the NF was soaked into 1 M KOH for 3 h for pre-activation. The mass load of the active material on the NF was around 2~3 mg. The specific capacitance (F g^{-1}) can be calculated from the following Eq. (1)[24]:

$$C = \frac{I\Delta t}{m\Delta V} \quad (1)$$

where I, Δt, m, ΔV indicate the applied current (A), discharge time (s), the mass load of the active material (g) and the working potential (V), respectively.

In the Ni_3N-$Co_2N_{0.67}$/NC//AC asymmetric supercapacitor system, active carbon (AC) was applied as the negative electrode material, which was prepared using the same steps as the positive electrode. The mass of AC can be computed based on the charge balance equation showing as follows[25]:

$$\frac{m_+}{m_-} = \frac{C_- \times V_-}{C_+ \times V_+} \quad (2)$$

where m_+, m_-, C_+, C_-, V_+, V_- represent the mass (g), specific capacitance (F g^{-1}) and operating voltage window (V) of the positive and negative electrode, respectively.

In addition, the energy density (Wh kg^{-1}) and power density (W kg^{-1}) at different current densities were calculated from the following Eqs.[26]:

$$E = \frac{C\Delta V^2}{2 \times 3.6} \quad (3)$$

$$P = \frac{3600 \times E}{\Delta t} \quad (4)$$

where C, ΔV, Δt are the specific capacitance (F g^{-1}), working potential (V) and discharge time (s) of the device, respectively.

RESULTS AND DISCUSSION

As schemed in Figure 1, the complete synthesis route of Ni_3N-$Co_2N_{0.67}$/NC includes two steps. In the first hydrothermal process, TEOA could serve as an ideal solvent and more importantly as a ligand for metal complexes[27]. To avoid inhibition of the complex growth kinetics and nonuniform dispersion of the reaction system due to strong viscosity of TEOA, DI water was chosen as the only cosolvent. Initially, TEOA molecules react with Ni (II) and Co (II) to form Ni_xCo_y-TEOA complex at low temperatures. With the temperature rising, this metal alkoxide begins to hydrolyze, leading to the hollow porous nanoflower structure[21]. In the subsequent thermal treatment, carbon skeleton is pyrolyzed at 400 °C and transformed to N-doped carbon owing to the existence of N center atom of TEOA. Simultaneously, urea decomposes into NH_3 which further reacts with Ni (II) and Co (II), producing Ni_3N and $Co_2N_{0.67}$ eventually. Additionally, various mass ratios of Ni^{2+} to Co^{2+} (0:3, 1:2, 1:1, 2:1, 3:0) were used to investigate the impact on morphology and electrochemical performance of the complex and the best one was chosen to further derivative to the final product.

XRD patterns of N_0C_3-TEOA, N_1C_2-TEOA, N_1C_1-TEOA, N_2C_1-TEOA and N_3C_0-TEOA are presented in Supplementary Figure 1. As expected, all the precursors show no sharp and distinct peaks, exhibiting salient amorphous characteristics[28]. The wide peak bulge at 15°-25° is assigned to the (002) crystal face of carbon, indicating the successful formation of nitrogen-doped carbon after calcining [Figure 2A][29]. The peaks at 38.9°, 42.1°, 44.5°, 58.5°, 70.6° and 78.4° could be attributed to the (110), (002), (111), (112), (300) and (113)

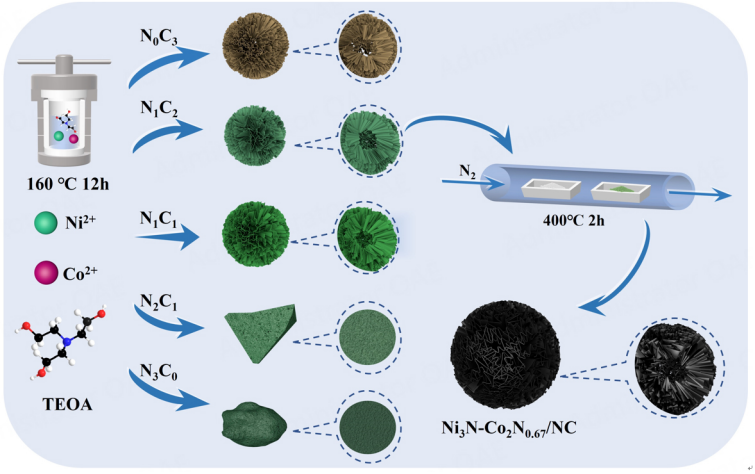

Figure 1. Schematic illustration of preparation process of Ni_3N-$Co_2N_{0.67}$/NC.

crystal faces of Ni_3N (JCPDS:06-0691), while the peaks at 39.0°, 41.6°, 44.4°, 58.2°, 70.7° and 77.7° could correspond to the (100), (002), (101), (102), (110) and (103) crystal faces of $Co_2N_{0.67}$ (JCPDS:10-0280). All these peaks are sharp and narrow due to the good crystallinity of the material[30]. Moreover, no peaks were observed for nickel oxide or cobalt oxide, suggesting pristine metal nitrides were obtained.

The morphologies of precursors were investigated by SEM as displayed in Supplementary Figure 2A-J. N_0C_3-TEOA, N_1C_2-TEOA, and N_1C_1-TEOA are all hollow nanoflower shapes with self-assembled petal-like nanosheets and inner hollow space. However, with the increase of Ni ratio, the radius of these nanoflowers decrease gradually. The radius of N_0C_3-TEOA is about 1.5 μm, while the radius of N_1C_2-TEOA and N_1C_1-TEOA dwindle to 1 μm and 500 nm, respectively. When the Ni ratio further increases (N_2C_1-TEOA and N_3C_0-TEOA), the morphology and structure collapse to irregular shapes and expand greatly in size with a rough surface, which might be an important reason for their poor electrochemical performance. As plotted in Figure 2B and C, Ni_3N-$Co_2N_{0.67}$/NC maintain the hollow nanoflower-like structure with a radius of around 1 μm, revealing that the nitridation process did not destroy the sample's initial morphology. All the nanoflowers are distributed uniformly without excessive agglomerations or clustering. Interestingly, more pores were created during thermal treatment due to the gas escape during carbon decomposition, which greatly increases the specific surface area, providing plentiful active sites for redox reactions.

TEM was employed to gain a better understanding of the internal microstructure of Ni_3N-$Co_2N_{0.67}$/NC. As can be seen in Figure 2D, Ni_3N-$Co_2N_{0.67}$/NC shows a typical nanoflower structure with a hollow inner core, which is well consistent with SEM images. HRTEM was then carried out to analyze the composition of Ni_3N-$Co_2N_{0.67}$/NC. The black circular area and the white background in Figure 2E are metal nitrides and NC, respectively. SAED in the inset of Figure 2E reveals a typical polycrystalline characteristic[31]. The lattice ring is assigned to the (101) and (111) crystal faces of $Co_2N_{0.67}$ and Ni_3N, respectively. The result is further confirmed in Figure 2F. The interplanar spacing of 0.202 nm and 0.204 nm correspond well with (111) and (101) crystal faces of Ni_3N and $Co_2N_{0.67}$/NC, which is consistent with the XRD result. The EDS mapping images in Figure 2H-L swept from the HAADF TEM image in Figure 2G reveal uniform dispersion of Ni, Co, C, N and O elements. Furthermore, EDS spectrum in Figure 2M display the peaks corresponding to Ni, Co, C, N and O and their atomic fraction are 6.38%, 13.16%, 52.46%, 9.93% and 18.07%, respectively. The atomic number ratio of Ni and Co of Ni_3N-$Co_2N_{0.67}$/NC are the same as designed.

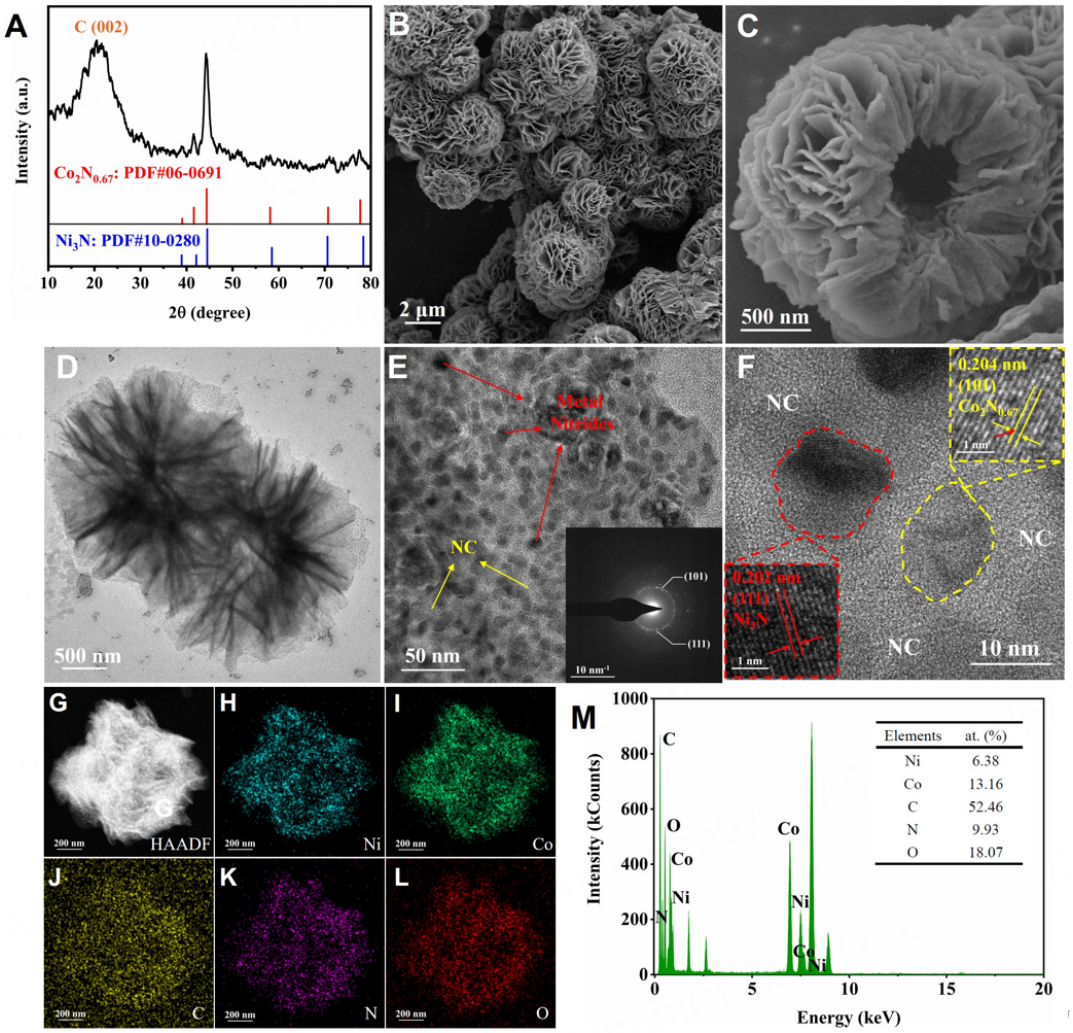

Figure 2. (A) XRD pattern of Ni_3N-$Co_2N_{0.67}$/NC. (B and C) SEM images of Ni_3N-$Co_2N_{0.67}$/NC. (D) TEM image. (E and F) high-resolution TEM image (Inset: SAED image). (G) high-angle annular dark field TEM image. (H and L) the EDS mapping images of Ni, Co, C, N, and O elements. (M) EDS diagram. XRD: X-ray diffraction; SEM: scanning electron microscopy; TEM: transmission electron microscopy; SAED: selected area electron diffraction.

To investigate the pore nature of the precursors and Ni_3N-$Co_2N_{0.67}$/NC, N_2 adsorption-desorption measurement was conducted, as shown in Supplementary Figure 3A-D and Figure 3A. All the isotherms belong to type IV, indicating their mesoporous characteristics[32]. The specific surface areas of N_0C_3-TEOA, N_1C_2-TEOA, N_1C_1-TEOA, N_2C_1-TEOA and N_3C_0-TEOA are found to be 18.88 m^2g^{-1}, 20.98 m^2g^{-1}, 18.35 m^2g^{-1}, 1.573 m^2g^{-1} and 0.844 m^2g^{-1}, respectively. With the nanoflower structure destroyed, the specific surface areas sharply decrease and the number of pores with a diameter larger than 30 nm reduces for N_2C_1-TEOA and N_3C_0-TEOA, which is identical to the SEM results shown in Supplementary Figure 2G and H. As expected, the specific surface area rises to 24.35 m^2g^{-1} due to the numerous pores created by the formation of porous carbon via pyrolysis. Moreover, it can be concluded from the pore size distribution pattern in the inset of Figure 3A that various sizes of pores exist, the main of which are mesopores. The favored specific area benefits from the self-assembled nanosheets and abundant pores, which not only provide fast diffusion channels for ions/electrons but offer sufficient sites for redox reactions.

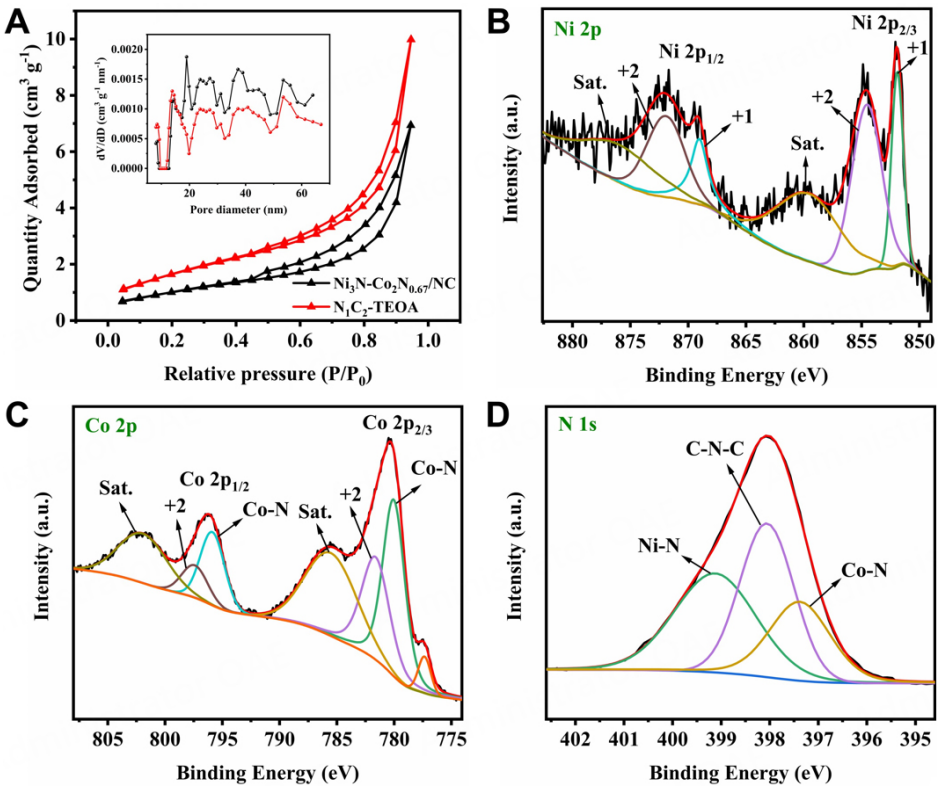

Figure 3. (A) N_2 adsorption-desorption isotherms of Ni_3N-$Co_2N_{0.67}$/NC and N_1C_2-TEOA (Inset: pore size distribution pattern). High-resolution XPS spectrum and simulation of (B) Ni 2p, (C) Co 2p and (D) N 1s for Ni_3N-$Co_2N_{0.67}$/NC.

The changes in chemical bonds are characterized by FTIR exhibited in Supplementary Figure 4. The peaks at around 3400 cm^{-1} are ascribed to the -OH group of adsorbed water molecules[33]. For the precursors, the peaks at about 2842-3062 cm^{-1} are related to the stretching vibration of -CH_2-, while the peaks at 1342-1533 cm^{-1} correspond to the bending vibration of -CH-. The peak at 1223 cm^{-1} is assigned to the C-N bond[34]. The peaks at around 917 cm^{-1} and 1633 cm^{-1} can be indexed to the stretching vibrations of C-O[35]. The peaks at around 974-1155 cm^{-1} are ascribed to the C-C bond. Moreover, the peak at 649 cm^{-1} belongs to the bending vibration of metal-O-metal groups, suggesting the successful formation of metal complex[36]. Rationally, most bonds mentioned above disappeared or shrank after calcining, revealing the carbonization of ligand skeleton. It can be concluded from the above data that metal-TEOA complex was formed as expected, which was transformed into metal nitrides/NC via pyrolysis. The rigid carbon skeleton can prevent the material from deformation and enhance conductivity. Furthermore, promoted number of exposure sites are offered by the considerable pores, achieving the material with large specific surface area and fast transportation channel.

XPS was determined to observe the surficial element and electronic interaction. Supplementary Figure 5 demonstrates the survey spectra of Ni_3N-$Co_2N_{0.67}$/NC, evidencing the presence of Ni, Co, C, N and O elements. For the Ni 2p spectra in Figure 3B, the peaks located at 854.57 and 871.94 eV are attributed to oxidized Ni^{2+}, while the peaks centered at 851.92 and 869.04 eV can be indexed to Ni^{+} species of Ni-N bonds[37]. For the Co 2p spectra in Figure 3C, the peaks at 781.62 and 797.41 eV are assigned to Co^{2+} and the peaks at 780.03 and 795.86 eV are caused by Co-N bonds[38]. The results above reveal the existence of Ni_3N and $Co_2N_{0.67}$, which is further proved in N 1 s spectra in Figure 3D. The peaks at 399.12 and 397.38 eV belong to Ni-N and Co-N bonds, respectively[39,40]. Moreover, the peak at 398.06 corresponds to C-N-C

groups, suggesting the successful establishment of nitrogen-doped carbon network[41]. Nitrogen doping could enhance the electrical conductivity of carbon, thus improving the energy storage performance of Ni_3N-$Co_2N_{0.67}$[42].

The electrochemical performances of all the samples were conducted in a three-electrode system in 1 M KOH aqueous electrolyte. As plotted in Figure 4A, the CV curves of all the samples at 20 mV s^{-1} show distinct redox peaks, revealing their energy storage mechanism of the combination of pseudocapacitance and double-layer capacitance[43]. To choose the best precursor for further nitridation, we initially compared the specific capacitance of all the precursors. The galvanostatic charge-discharge (GCD) profiles at 1 A g^{-1} displayed in Figure 4B of all the precursors show evident charge-discharge plateaus, which is well consistent with CV result. Interestingly, N_1C_1-TEOA and N_2C_1-TEOA could only reach a working potential window of 0.3 V with capacitances of 647 and 873 F g^{-1}, respectively. N_0C_3-TEOA, N_1C_2-TEOA and N_3C_0-TEOA could reach a working potential window of 0.5 V with capacitances of 158, 972 and 382 F g^{-1}, respectively. Obviously, N_1C_2-TEOA exhibited the best capacitive performance among the precursors and owned a favorable structure, so it was chosen for further annealing. As expected, Ni_3N-$Co_2N_{0.67}$/NC possessed the longest discharge time and an operating potential window of 0.5 V, surpassing all the precursors. Electrochemical impedance spectroscopy (EIS) was measured to figure out the charge transfer and ion diffusion mechanism of the samples in the frequency range from 100 kHz to 0.01 Hz. The curve in Figure 4C consists of three regions. The charge transfer resistance (R_{ct}) is determined by the diameter of the semicircle in the high-frequency region, while the diffusion resistance (R_w) of ions can be obtained from the linear slope of the straight line in the low-frequency region. As for the intercept of the curve in the high-frequency region, it means the series resistance (R_s) of the inductive element[44,45]. Benefiting from the excellent conductivity of metal nitrides and nitrogen-doped carbon, the curve of Ni_3N-$Co_2N_{0.67}$/NC owns the largest slope in the high-frequency region. Figure 4D shows the CV curve of Ni_3N-$Co_2N_{0.67}$/NC at different sweep rates. The curves almost maintain the initial shape with the scan rate increasing from 10 mV s^{-1} to 50 mV s^{-1}, indicating steady rate ability[46]. Moreover, the redox peaks sightly move to both sides of X axis when the scan rate increases due to the enhancement of internal resistance[47]. Based on the GCD profiles in Figure 4E, the specific capacitances of Ni_3N-$Co_2N_{0.67}$/NC at 1, 2, 3, 4, 5, 10 and 20 A g^{-1} are calculated as 1582, 1344, 1230, 1144, 1080, 860 and 840 F g^{-1} [Figure 4F], superior to other similar material reported previously in Supplementary Table 1. Even at a high current density of 20 A g^{-1}, the specific capacitance still preserves 53.1% of the initial value, reconfirming its outstanding rate capacity. The cycle life of Ni_3N-$Co_2N_{0.67}$/NC was tested at 10 A g^{-1}. As shown in Figure 4G, 83.79% capacitance retention can be reached after 5000 cycles. The good stability originated from the strong support of rigid carbon skeleton. To gain further insight into the electrochemical reaction kinetics of Ni_3N-$Co_2N_{0.67}$/NC, the capacitive contribution was calculated according to the following Eq.[48]:

$$i = av^b \tag{5}$$

where i and v represent peak current and scan rate, respectively. a and b are constants. The b value can be calculated through the slope of log(i) versus log(v). A b value of 0.5 means the process is a diffusion-controlled process, while a b value of 1 demonstrates a surface-controlled process[49]. The b value of Ni_3N-$Co_2N_{0.67}$/NC displays 0.68 and 0.70 from the cathodic and anodic peaks, respectively, which implies a combination of surface-controlled and diffusion-controlled processes [Figure 4H]. Further analysis of capacitive contribution ratio was conducted based on the following Eq.[50]:

$$i = k_1 v + k_2 v^{\frac{1}{2}} \tag{6}$$

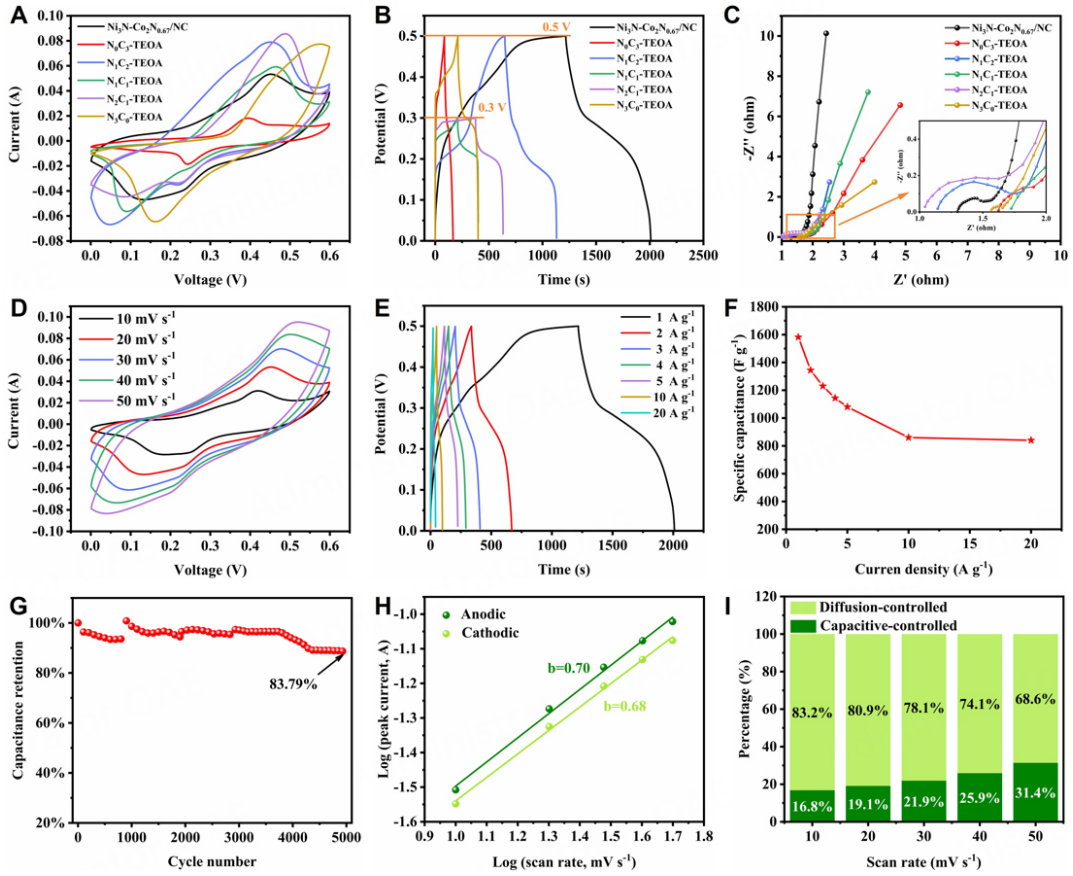

Figure 4. (A) CV curves, (B) GCD profiles and (C) Nyquist plots in the frequency range from 100 kHz to 0.01 Hz of Ni_3N-$Co_2N_{0.67}$/NC, N_0C_3-TEOA, N_1C_2-TEOA, N_1C_1-TEOA, N_2C_1-TEOA, N_3C_0-TEOA. (D) CV curves at different scan rates and (E) GCD profiles at different current densities of Ni_3N-$Co_2N_{0.67}$/NC. (F) Specific capacitance of Ni_3N-$Co_2N_{0.67}$/NC calculated from GCD profiles at different current densities. (G) The cycle performance curve of Ni_3N-$Co_2N_{0.67}$/NC at 10 A g^{-1}. (H) *b* values simulated from anodic and cathodic peak current and scan rate of Ni_3N-$Co_2N_{0.67}$/NC. (I) Contribution ratio between capacitance and the diffusion-controlled process under various scan rates.

where *i*, *v*, k_1 and k_2 are current, scan rate and determined parameters. The capacitive contribution area (green) inside CV curves at different scan rates for Ni_3N-$Co_2N_{0.67}$/NC are presented in Supplementary Figure 6A-E. Based on these plots, the percentage contribution of diffusion- and capacitive-controlled processes at different sweep rates is shown in Figure 4I. The capacitive-controlled percentage slightly rises with the increase in scan rate, confirming the excellent rate performance of Ni_3N-$Co_2N_{0.67}$/NC[51].

To explore the practical application of Ni_3N-$Co_2N_{0.67}$/NC electrode, an asymmetric device was configured applying Ni_3N-$Co_2N_{0.67}$/NC and active carbon as positive and negative electrodes in 1 M KOH, respectively. The scheme of the Ni_3N-$Co_2N_{0.67}$/NC//AC asymmetric supercapacitor (ASC) is shown in Figure 5A. CV curves and GCD profiles of AC were measured in Supplementary Figure 7A and B to determine the working potential window and mass ratio of positive electrode to negative electrode of the device. The mass ratio of Ni_3N-$Co_2N_{0.67}$/NC to AC was calculated to be 0.18 and the working potential widow was estimated to be 1.6 V based on the CV curve of Ni_3N-$Co_2N_{0.67}$/NC and AC at 20 mV s^{-1} [Figure 5B]. To further define the operating potential window, CV curves at 20 mV s^{-1} and GCD profiles at 1 A g^{-1} at different operating voltages were performed [Figure 5C and D]. The CV curve met a significant polarization when the

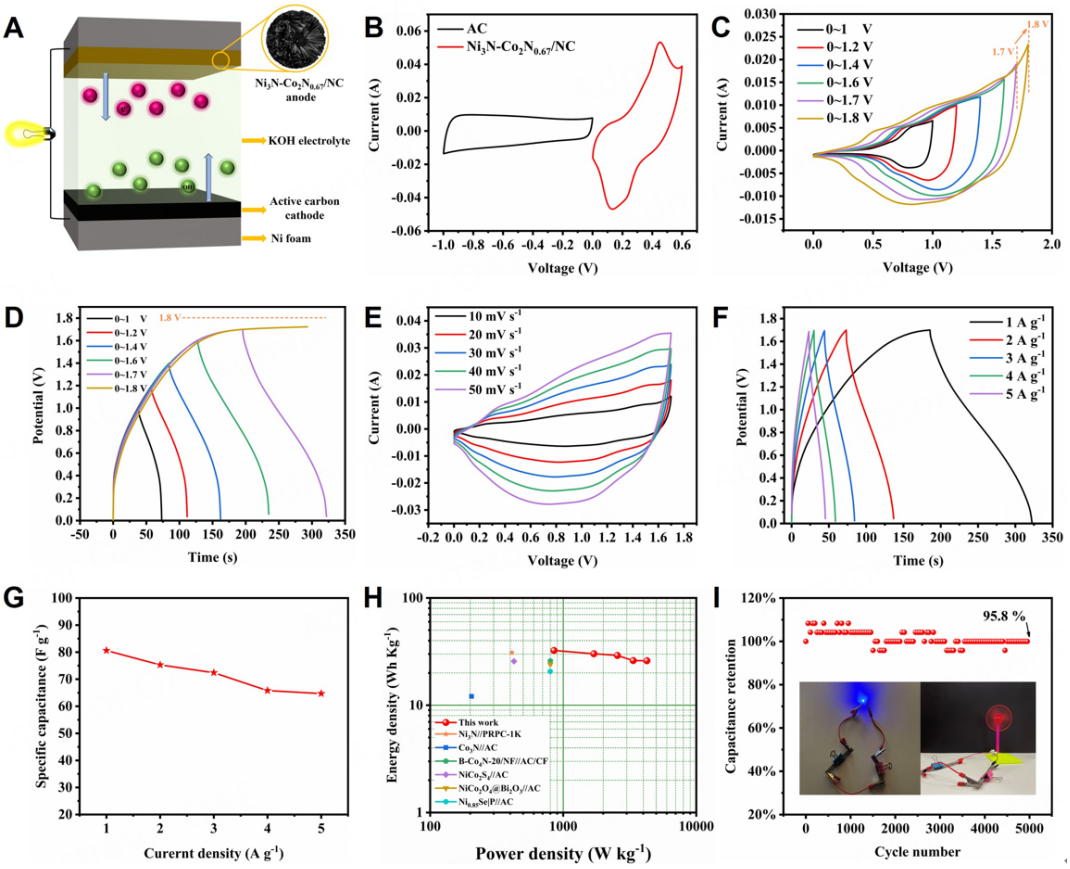

Figure 5. (A) Scheme of Ni_3N-$Co_2N_{0.67}$/NC//AC asymmetric supercapacitor. (B) CV curves of Ni_3N-$Co_2N_{0.67}$/NC and AC at 20 mV s^{-1}. (C) CV curves of Ni_3N-$Co_2N_{0.67}$/NC//AC ASC at different voltage ranges at 20 mV s^{-1}. (D) GCD profiles of Ni_3N-$Co_2N_{0.67}$/NC//AC ASC at different voltage ranges at 1 A g^{-1}. (E) CV curves of Ni_3N-$Co_2N_{0.67}$/NC//AC ASC at different scan rates. (F) GCD profiles of Ni_3N-$Co_2N_{0.67}$/NC//AC ASC at different current densities. (G) Specific capacitance of Ni_3N-$Co_2N_{0.67}$/NC//AC ACS calculated from GCD test. (H) Ragone plots comparing the Ni_3N-$Co_2N_{0.67}$/NC//AC with other similar electrode materials. (I) Cycle performance of Ni_3N-$Co_2N_{0.67}$/NC//AC ASC at 10 A g^{-1} (Inset: the photo of two ASC devices connected in series to light a LED bulb and to rotate a fan).

operating voltage increased from 1.7 V to 1.8 V and the GCD profile could only reach 1.7 V, so 1.7 V was finally selected as the practical working potential window. CV curves of the ACS at different sweep rates display a pair of redox peaks and remain stable, suggesting Faraday redox characteristics and superior rate capability [Figure 5E]. Calculated from GCD profiles in Figure 5F, the device demonstrates specific capacitance of 80.6, 75.3, 72.4, 65.8 and 64.7 F g^{-1} at 1, 2, 3, 4 and 5 A g^{-1} [Figure 5G]. The capacitance remains 80.3% of its initial value when the current density reaches 5 A g^{-1}, indicating excellent capacitive performance. The ASC device delivers a maximum energy density of 32.4 W h Kg^{-1} at a power density of 851.3 W Kg^{-1}. Even at the maximum power density of 4254.5 W Kg^{-1}, the energy density is still 26 W h Kg^{-1}, surpassing other similar devices reported before such as Ni_3N//PRPC-1k[52], Co_3N//AC[53], B-Co_4N-20/NF//AC/CF[54], $NiCo_2S_4$//AC[55], $NiCo_2O_4$@Bi_2O_3//AC[56] and $Ni_{0.85}Se$|P//AC[57] [Figure 5H]. After 5000 cycles at 10 A g^{-1}, the ASC device exhibited ultrahigh capacitance retention of 95.8% [Figure 5I]. The enhanced cycle performance of the device over a single electrode in the three electrodes system arises from the stable structure and long cycle life of AC electrode[58]. In addition, a LED bulb can be lighted for about 2 min and a small fan can be rotated for around 1 min with two ASC devices in series, showing its potentially broad applications (Insets of Figure 5I).

CONCLUSIONS

In conclusion, hollow Ni_3N-$Co_2N_{0.67}$/NC nanoflower was synthesized by pyrolyzing nickel/cobalt-TEOA complex precursor using urea as the nitrogen source and applied as positive electrode material for supercapacitor. Thanks to the remarkable electronic conductivity originating from metal nitrides and N-doped carbon and copious active sites provided by self-assembled nanosheets and porous structure, the Ni_3N-$Co_2N_{0.67}$/NC exhibits appreciable electrochemical performance. In a three-electrode system, the Ni_3N-$Co_2N_{0.67}$/NC delivers a high specific capacitance of 1582 F g^{-1} at 1 A g^{-1} and excellent cycle stability (83.79% after 5000 cycles at 10 A g^{-1}). Additionally, when fabricated as Ni_3N-$Co_2N_{0.67}$/NC//AC ASC device, it displays a favorable energy density of 32.4 W h Kg^{-1} at a power density of 851.3 W Kg^{-1} and outstanding capacitance retention (95.8% after 5000 cycles at 10 A g^{-1}). This work may create ideas to prepare metal nitride-based nanomaterials using nontoxic nitrogen source and pave the way for the rational design of hollow inorganic materials/carbon composites with high performance for SCs.

DECLARATIONS

Authors' contributions

Designed the study and supervised the overall project: Zhu M
Performed the experiments, collected data, and drafted the manuscript: Luo Q
Contributed to the result discussion: Luo Q, Lu C, Liu L, Zhu M

Availability of data and materials

Not applicable.

Financial support and sponsorship

The authors acknowledge the financial support from the Nation Natural Science Foundation of China (21403091).

Conflicts of interest

All authors declared that there are no conflicts of interest.

Ethical approval and consent to participate

Not applicable.

Consent for publication

Not applicable.

REFERENCES

1. Wu S, Chen Y, Jiao T, et al. An aqueous Zn-Ion hybrid supercapacitor with high energy density and ultrastability up to 80,000 cycles. *Adv Energy Mater* 2019;9:1902915. DOI
2. Yu Z, Duong B, Abbitt D, Thomas J. Highly ordered MnO_2 nanopillars for enhanced supercapacitor performance. *Adv Mater* 2013;25:3302-6. DOI PubMed
3. Ji J, Zhang LL, Ji H, et al. Nanoporous $Ni(OH)_2$ thin film on 3D Ultrathin-graphite foam for asymmetric supercapacitor. *ACS Nano* 2013;7:6237-43. DOI PubMed
4. Dubal DP, Ayyad O, Ruiz V, Gómez-Romero P. Hybrid energy storage: the merging of battery and supercapacitor chemistries. *Chem Soc Rev* 2015;44:1777-90. DOI PubMed
5. Xu B, Zhang H, Mei H, Sun D. Recent progress in metal-organic framework-based supercapacitor electrode materials. *Coord Chem Rev* 2020;420:213438. DOI
6. Ma R, Chen Z, Zhao D, et al. $Ti_3C_2T_x$ MXene for electrode materials of supercapacitors. *J Mater Chem A* 2021;9:11501-29. DOI

7. Li K, Zhao B, Zhang H, et al. 3D porous honeycomb-like CoN-Ni_3N/N-C nanosheets integrated electrode for high-energy-density flexible supercapacitor. *Adv Funct Mater* 2021;31:2103073. DOI
8. Meng L, Bi J, Gao X, et al. Heterostructure Co_2N-Ni_3N/NF nanoarrays synthesized by in situ nitriding treatment for high-performance supercapacitor. *J Alloys Compd* 2022;909:164721. DOI
9. Zhu C, Sun Y, Chao D, et al. A 2.0 V capacitive device derived from shape-preserved metal nitride nanorods. *Nano Energy* 2016;26:1-6. DOI
10. Xiao X, Peng X, Jin H, et al. Freestanding mesoporous VN/CNT hybrid electrodes for flexible all-solid-state supercapacitors. *Adv Mater* 2013;25:5091-7. DOI PubMed
11. Xiao X, Yu H, Jin H, et al. Salt-templated synthesis of 2D metallic mon and other nitrides. *ACS Nano* 2017;11:2180-6. DOI PubMed
12. Wang H, Li J, Li K, et al. Transition metal nitrides for electrochemical energy applications. *Chem Soc Rev* 2021;50:1354-90. DOI PubMed
13. Yang H, Ning P, Cao H, et al. Selectively anchored vanadate host for self-boosting catalytic synthesis of ultra-fine vanadium nitride/nitrogen-doped hierarchical carbon hybrids as superior electrode materials. *Electrochim Acta* 2020;332:135387. DOI
14. Jin T, Sang X, Unocic RR, et al. Mechanochemical-assisted synthesis of high-entropy metal nitride via a soft urea strategy. *Adv Mater* 2018;30:e1707512. DOI PubMed
15. Patra S, Roy E, Madhuri R, Sharma PK. Agar based bimetallic nanoparticles as high-performance renewable adsorbent for removal and degradation of cationic organic dyes. *J Ind Eng Chem* 2016;33:226-38. DOI
16. Patra S, Roy E, Madhuri R, Sharma PK. Nanocomposite of bimetallic nanodendrite and reduced graphene oxide as a novel platform for molecular imprinting technology. *Anal Chim Acta* 2016;918:77-88. DOI PubMed
17. Aziz ST, Kumar S, Riyajuddin S, Ghosh K, Nessim GD, Dubal DP. Bimetallic phosphides for hybrid supercapacitors. *J Phys Chem Lett* 2021;12:5138-49. DOI PubMed
18. Ren F, Ji Y, Chen F, Qian Y, Tian J, Wang J. Flower-like bimetal Ni/Co-based metal-organic-framework materials with adjustable components toward high performance solid-state supercapacitors. *Mater Chem Front* 2021;5:7333-42. DOI
19. Huang K, Sun Y, Zhang Y, Wang X, Zhang W, Feng S. Hollow-structured metal oxides as oxygen-related catalysts. *Adv Mater* 2019;31:e1801430. DOI PubMed
20. Zhu M, Cheng Y, Luo Q, El-khateeb M, Zhang Q. A review of synthetic approaches to hollow nanostructures. *Mater Chem Front* 2021;5:2552-87. DOI
21. Liu X, Deng S, Xiao D, et al. Hierarchical bimetallic Ni-Co-P microflowers with ultrathin nanosheet arrays for efficient hydrogen evolution reaction over all pH values. *ACS Appl Mater Interfaces* 2019;11:42233-42. DOI PubMed
22. Dong J, Lu G, Yue J, Cheng Z, Kang X. Valence modulation in hollow carbon nanosphere/manganese oxide composite for high performance supercapacitor. *Appl Surf Sci* 2019;480:1116-25. DOI
23. Yang Y, Shao Z. Boron and nitrogen co-doped carbon nanospheres for supercapacitor electrode with excellent specific capacitance. *Nanotechnology* 2022;33:185403. DOI PubMed
24. Yang M, Ning H, Xiao L, Cui F, Zhang F. Mn_3O_4/MnS heterostructure for electrode and asymmetric supercapacitor under high charge/discharge current. *Electrochim Acta* 2022;424:140630. DOI
25. Qiu L, Yang W, Zhao Q, et al. NiS nanoflake-coated carbon nanofiber electrodes for supercapacitors. *ACS Appl Nano Mater* 2022;5:6192-200. DOI
26. Ran F, Yang X, Xu X, Li S, Liu Y, Shao L. Green activation of sustainable resources to synthesize nitrogen-doped oxygen-riched porous carbon nanosheets towards high-performance supercapacitor. *Chem Eng J* 2021;412:128673. DOI
27. Liang J, Li M, Chai Y, Luo M, Li L. TEOA-mediated formation of hollow core-shell structured $CoNi_2S_4$ nanospheres as a high-performance electrode material for supercapacitors. *J Power Sources* 2017;362:123-30. DOI
28. Chen Y, Yang D, Xin X, et al. Multi-stepwise charge transfer via MOF@MOF/TiO_2 dual-heterojunction photocatalysts towards hydrogen evolution. *J Mater Chem A* 2022;10:9717-25. DOI
29. Zhang H, Yao Z, Lan D, Liu Y, Ma L, Cui J. N-doped carbon/V_2O_3 microfibers as high-rate and ultralong-life cathode for rechargeable aqueous zinc-ion batteries. *J Alloys Compd* 2021;861:158560. DOI
30. Rezaei B, Hansen TW, Keller SS. Stereolithography-derived three-dimensional pyrolytic carbon/Mn_3O_4 nanostructures for free-standing hybrid supercapacitor electrodes. *ACS Appl Nano Mater* 2022;5:1808-19. DOI
31. Xing M, Gao A, Liang Y, et al. Defect-engineered 3D cross-network $Co_3O_{4-x}N_x$ nanostructure for high-performance solid-state asymmetric supercapacitors. *ACS Appl Energy Mater* 2021;4:888-98. DOI
32. Rabani I, Zafar R, Subalakshmi K, Kim HS, Bathula C, Seo YS. A facile mechanochemical preparation of Co_3O_4@g-C_3N_4 for application in supercapacitors and degradation of pollutants in water. *J Hazard Mater* 2021;407:124360. DOI
33. Vanaraj R, Vinodh R, Periyasamy T, et al. Capacitance enhancement of metal-organic framework (MOF) materials by their morphology and structural formation. *Energy Fuels* 2022;36:4978-91. DOI
34. Chen L, Huang Z, Liang H, Gao H, Yu S. Three-dimensional heteroatom-doped carbon nanofiber networks derived from bacterial cellulose for supercapacitors. *Adv Funct Mater* 2014;24:5104-11. DOI
35. Dong Z, Zhang W, Xiao Y, et al. One-pot-synthesized CoFe-glycerate hollow spheres with rich oxyhydroxides for efficient oxygen evolution reaction. *ACS Sustain Chem Eng* 2020;8:5464-77. DOI
36. Zhao J, Zou XX, Su J, Wang PP, Zhou LJ, Li GD. Synthesis and photocatalytic activity of porous anatase TiO_2 microspheres composed of {010}-faceted nanobelts. *Dalton Trans* 2013;42:4365-8. DOI PubMed

37. Hua W, Sun H, Liu H, Li Y, Wang J. Interface engineered NiMoN/Ni_3N heterostructures for enhanced alkaline hydrogen evolution reaction. *Appl Surf Sci* 2021;540:148407. DOI
38. Hu Y, Luo Z, Guo M, et al. Interface engineering of $Co_2N_{0.67}$/$CoMoO_4$ heterostructure nanosheets as a highly active electrocatalyst for overall water splitting and Zn-H_2O cell. *Chem Eng J* 2022;435:134795. DOI
39. Sun J, Lu J, Huang C, et al. Modification of Ni_3N with a cobalt-doped carbon shell for high-performance hydrogen evolution in alkaline media. *ACS Sustain Chem Eng* 2021;9:1994-2002. DOI
40. Tong R, Xu M, Huang H, et al. $Co_2N_{0.67}$/MoO_2 heterostructure as high-efficiency electrocatalysts for the hydrogen evolution reaction. *ACS Appl Energy Mater* 2022;5:440-8. DOI
41. Wang M, Ma W, Lv Z, Liu D, Jian K, Dang J. Co-doped Ni_3N nanosheets with electron redistribution as bifunctional electrocatalysts for efficient water splitting. *J Phys Chem Lett* 2021;12:1581-7. DOI PubMed
42. Inagaki M, Toyoda M, Soneda Y, Morishita T. Nitrogen-doped carbon materials. *Carbon* 2018;132:104-40. DOI
43. Shi B, Li L, Chen A, Jen TC, Liu X, Shen G. Continuous fabrication of $Ti_3C_2T_x$ MXene-based braided coaxial Zinc-Ion hybrid supercapacitors with improved performance. *Nanomicro Lett* 2021;14:34. DOI
44. Ma J, Xia J, Liang Z, Chen X, Du Y, Yan CH. Layered double hydroxide hollowcages with adjustable layer spacing for high performance hybrid supercapacitor. *Small* 2021;17:e2104423. DOI PubMed
45. Wang J, Huang Y, Han X, Li Z, Zhang S, Zong M. A flexible Zinc-Ion hybrid supercapacitor constructed by porous carbon with controllable structure. *Appl Surf Sci* 2022;579:152247. DOI
46. Peçenek H, Dokan FK, Onses MS, Yılmaz E, Sahmetlioglu E. Outstanding supercapacitor performance with intertwined flower-like NiO/MnO_2/CNT electrodes. *Mater Res Bull* 2022;149:111745. DOI
47. Wang H, Liang M, Duan D, Shi W, Song Y, Sun Z. Rose-like Ni_3S_4 as battery-type electrode for hybrid supercapacitor with excellent charge storage performance. *Chem Eng J* 2018;350:523-33. DOI
48. Houpt D, Ji J, Yang D, Choi JH. High-performance supercapacitor electrodes based on composites of MoS_2 nanosheets, carbon nanotubes, and ZIF-8 metal-organic framework nanoparticles. *ACS Appl Nano Mater* 2022;5:1491-9. DOI
49. Yesuraj J, Vajravijayan S, Yang R, et al. Self-assembly of hausmannite Mn_3O_4 triangular structures on cocosin protein scaffolds for high energy density symmetric supercapacitor application. *Langmuir* 2022;38:2928-41. DOI
50. Li H, Liu T, He Y, et al. Interfacial engineering and a low-crystalline strategy for high-performance supercapacitor negative electrodes: $Fe_2P_2O_7$ nanoplates anchored on N/P co-doped graphene nanotubes. *ACS Appl Mater Interfaces* 2022;14:3363-73. DOI
51. Kim SJ, Sharma V, Kshetri T, Kim NH, Lee JH. Freestanding binder-free electrodes with nanodisk-needle-like MnCuCo-LTH and $Mn_1Fe_2S_2$ porous microthorns for high-performance quasi-solid-state supercapacitors. *ACS Appl Mater Interfaces* 2022;14:12523-37. DOI
52. Peng H, Dai X, Sun K, et al. A high-performance asymmetric supercapacitor designed with a three-dimensional interconnected porous carbon framework and sphere-like nickel nitride nanosheets. *New J Chem* 2019;43:12623-9. DOI
53. Gao J, Zhang W, Zhao Z, Kong L. Solid-phase synthesis and electrochemical pseudo-capacitance of nitrogen-atom interstitial compound Co_3N. *Sustain Energy Fuels* 2018;2:1178-88. DOI
54. Wang Z, Qu G, Wang C, et al. Modified Co_4N by B-doping for high-performance hybrid supercapacitors. *Nanoscale* 2020;12:18400-8. DOI PubMed
55. Wang M, An L, Wu M, et al. Self-template synthesis of nickel cobalt sulfide hollow nanotubes for high-performance battery-type supercapacitors. *J Electrochem Soc* 2021;168:060510. DOI
56. Yu Z, Wang S, Huang Y, et al. Bi_2O_3 nanosheet-coated $NiCo_2O_4$ nanoneedle arrays for high-performance supercapacitor electrodes. *J Energy Storage* 2022;55:105486. DOI
57. Zhang Y, Wang T, Wang Y, et al. Metal organic frameworks derived hierarchical hollow $Ni_{0.85}$Se|P composites for high-performance hybrid supercapacitor and efficient hydrogen evolution. *Electrochim Acta* 2019;303:94-104. DOI
58. Li B, He Z, Zhao J, Liu W, Feng Y, Song J. Advanced Se_3P_4@C anode with exceptional cycling life for high performance potassium-ion batteries. *Small* 2020;16:e1906595. DOI